Available online at www.sciencedirect.com

ScienceDirect

Acta Materialia 90 (2015) 77–87

Acta MATERIALIA

www.elsevier.com/locate/actamat

Numerical study of molten and semi-molten ceramic impingement by using coupled Eulerian and Lagrangian method

Zihang Zhu,[a] Spyros Kamnis[b] and Sai Gu[a,*]

[a]*The School of Energy, Environment and Agrifood, Cranfield University, College Road, Bedfordshire MK43 0AL, United Kingdom*
[b]*Monitor Coatings Limited, 2 Elm Road, West Chirton North Industrial Estate, North Shields, Tyne & Wear NE29 8SE, United Kingdom*

Received 28 November 2014; revised 3 February 2015; accepted 6 February 2015
Available online 6 March 2015

Abstract—Large temperature gradients are present within ceramic powder particles during plasma spray deposition due to their low thermal conductivity. The particles often impinge at the substrate in a semi-molten form which in turn substantially affects the final characteristics of the coating being formed. This study is dedicated to a novel modeling approach of a coupled Eulerian and Lagrangian (CEL) method for both fully molten and semi-molten droplet impingement processes. The simulation provides an insight to the deformation mechanism of the solid core YSZ and illustrates the freezing-induced break-up and spreading at the splat periphery. A 30 μm fully molten YSZ particle and an 80 μm semi-molten YSZ particle with different core sizes and initial velocity ranging from 100 to 240 m/s were examined. The flattened degree for both cases were obtained and compared with experimental and analytical data.

Keywords: Thermal spray; Semi-molten particles; Coupled Eulerian and Lagrangian method; Flattening degree

1. Introduction

Thermal spray technology encompasses several processes which are used to create performance enhancing coatings. The coatings are formed by heating and accelerating micro-sized and nano-sized particles toward a targeted substrate surface. These particles initially impact onto the substrate where they deform and adhere. The particles then impinge onto one another, building up the coating particle by particle in a lamellar structure. The degree of deformation of these particles and their adhesion strength at the substrate can be attributed to several factors, including: particle impact velocity, particle size, particle melt fraction, particle material properties, wetting of the substrate by molten particles, temperature of the substrate and substrate roughness.

With the development of smarter and more complex oxide ceramic film applications, such as the dye-sensitized solar cell and functionally graded bioactive coatings, a detailed understanding of the deposition process at the substrate is required in order to control the adhesion, cohesion and porosity of the coatings. By coupling the jet and particulate phases, numerical models are capable of simulating the transient velocity, temperature and phase content of the powders traveling through a thermal spray device. The thermal-physical state of an individual particle can therefore be predicted at the substrate surface which can then be relayed into a focused impingement model in order to simulate the impingement and buildup of the coating microstructure particle by particle. The most developed finite element simulations for unmelted, solid particle impingements can be found in [1,2] for copper powder deposited by cold spray, and in [3,4] for tungsten–carbide cobalt (WC–Co) powder deposited by HVOF combustion spray. By utilizing the Johnson–Cook strain hardening, temperature softening plasticity model, the deformation and stress of the solid metal particles could be captured. However, thermal plasma spray is commonly utilized to deposit oxide ceramics such as YSZ in the size range of 20–90 μm [5,6]. Depending on the initial size of the coating powder, some particles hit the substrate at a fully molten state. Meanwhile other particles larger than 60 μm [7], are partially molten with a solid core due to high plasma gas temperature and high temperature gradient of particles caused by the low thermal conductivity of ceramic powders.

Despite lack of detailed understanding for the deposition of semi-molten droplet impingement, little modeling and simulation work has been reported, given the challenges of solving both solid and liquid phases simultaneously. The rule-based approach in [8] presents an efficient and unique way of estimating the porosity created during the

* Corresponding author; e-mail: s.gu@cranfield.ac.uk

http://dx.doi.org/10.1016/j.actamat.2015.02.010
1359-6462/

coating buildup of molten and semi-molten droplets. However, this method is not able to capture the detailed physics during the particle impingement process. The works presented in [9] and [10] are limited to 2D simulations, without details such as substrate heat transfer and solidification respectively, which are crucial elements in determining the splat morphology. Furthermore, a central core is not modeled as a moving solid in both cases. In a more comprehensive work by Tabbara et al. [11] a semi-molten ceramic droplet with a moving solid core was simulated at a relatively low velocity. A temperature gradient within the particle was predefined and the whole deformation of the liquid shell was captured accurately in consort with the freezing-induced break-up mechanism at the splat periphery. Alavi et al. [12] considered the influence of phase change after the impact in conjunction with the influence of the core size on impact dynamics. Wu et al. [13] expanded the validity of the aforementioned models for higher impact velocities between 100 to 200 m/s. In all previous studies listed above, the Volume of the Fluid (VOF) approach was utilized assuming that the solid core behaves as a rigid body without considering possible deformation of the solid core and the substrate at impact.

According to Li et al. [14], brittle materials may possess ductile behavior under particular conditions such as very high temperature or high pressure. In this case, modeling the solid core as a rigid body may produce unrealistic results. Therefore, new approaches are required for simulating both the liquid and the solid part simultaneously in a coupled manner. This investigation is the first of its kind, to simulate a semi-molten droplet impingement using a coupled Eulerian and Lagrangian (CEL) approach for thermal spray applications. The 3-D study particularly examines the splash deposit of the liquid ceramic shell, and the deformation of the solid core and substrate. The results give an insight of the morphology of fully molten ceramic particle impact and illustrate how semi-molten ceramic particles behave under dynamic impact conditions. The flattening degree of the particles are obtained and compared with both experimental and analytical data.

2. Numerical method

In the first case of fully molten YSZ particle, a 30 μm particle, with an initial velocity of 190 m/s was generated based on real spray parameters provided by Vardelle et al. [5]. Owing to the axisymmetric nature of the normal impact process, only a quarter of the computational domain was simulated as shown in Fig. 1(a). The particle impacting velocity was increased progressively from 100 to 240 m/s and the flattening degree for each case was obtained. The second case of semi-molten particles was simulated based on the experimental findings provided by [7]. The particle diameter was set to 80 μm with several solid core diameters. Due to the low thermal conductivity of the YSZ material, a temperature gradient along the radius of the sphere particle develops during thermal spraying [11,15]. The liquid outer shell was assigned an initial temperature gradient as shown in Fig. 2. The temperature profile within the solid core and toward the center was assumed constant based on the particle temperature profile provided in our previous studies [11,15].

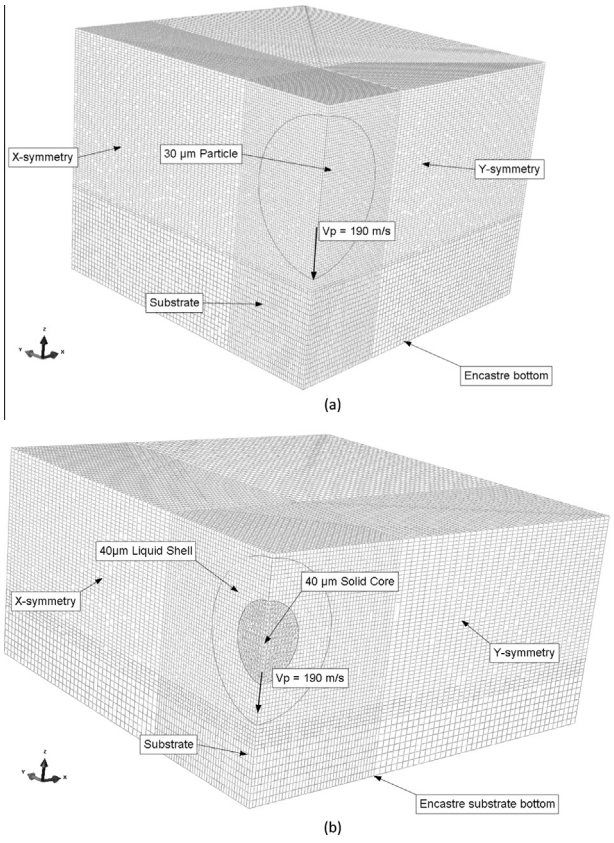

Fig. 1. (a) Computational model of molten particle impact benchmark. (b) Computational model of semi-molten particle impact with a core diameter of 60 μm.

The computational domain and mesh of semi-molten particle is illustrated in Fig. 1(b). In the explicit analysis, the stable time increment Δt_{stable} is given by:

$$\Delta t_{stable} < \frac{L_e}{C_d}$$

where L_e is the smallest element dimension and C_d is the wave speed in the material. The requirement for a fine mesh with small elements to capture the detailed physics of the process leads to very short maximum allowable time increments which, in turn, result in a computationally intensive analysis. In order to optimize the computational efficiency of the impact model, smaller elements were used only in the particle and along the particle–substrate interface. A mesh convergence study was carried out by varying the mesh density in the particle and along the contact interface. The mesh and geometry were generated using FEA software Abaqus/Explicit [16]. Given the velocity, viscosity, as well as characteristic length varying from case to case, the Reynolds Number in this paper will vary from 500 to 3000. The details of the mesh and solver could be found in Table 1.

2.1. Impingement model

The method for modeling the liquidus YSZ, Stainless Steel substrate, temperature profile, thermal and flow models is outlined below. The thermal-physical properties of the materials presented in this paper are summarized in Table 1.

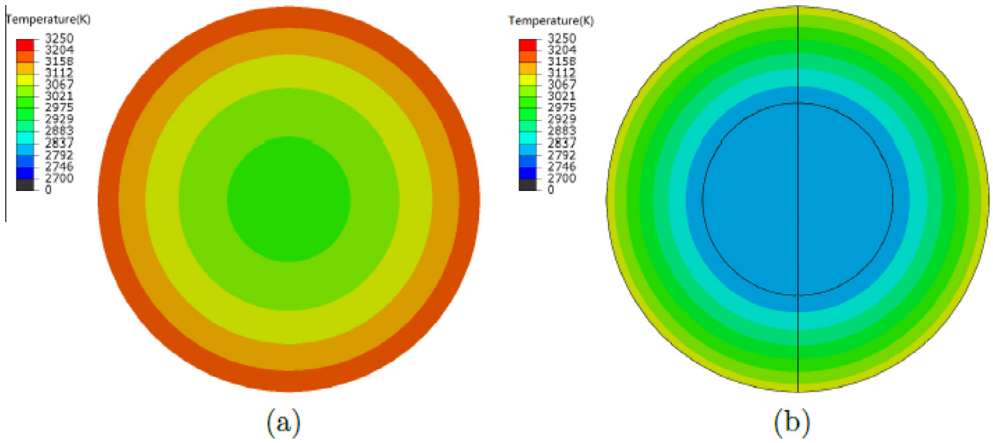

Fig. 2. (a) Initial temperature profile of liquid particle. (b) Initial temperature profile of semi-molten particle with a core diameter of 40 μm.

Table 1. Details of mesh and solver.

solver used	Abaqus/explicit
Element type for substrate	C3D8R
Order of accuracy	Second-order accuracy
Element type for solid YSZ	C3D8R
Order of accuracy	Second-order accuracy
Element type for liquid YSZ	EC3D8R
Order of accuracy	Second-order accuracy
No. of element for fully molten cases	855,300
No. of element for semi-molten cases	2,655,710

2.1.1. Mie–Grüneisen equation of state

The thermodynamic behavior model of real materials can be characterized by the following two-term relations [17]:

$$e(V,T) = e_{ref}(V) + e_T(V,T) \tag{1}$$

$$p(V,T) = p_{ref}(V) + \frac{\Gamma(V)}{V} e_T(V,T) \tag{2}$$

where $V = 1/\rho$ denotes the specific volume, T denotes the temperature, p is the pressure, e is the internal energy, and Γ is the Grüneisen parameter which represents the thermal pressure from a set of vibrating atoms. The p and e with subscription *ref* represent the pressure and internal energy at a reference state usually assumed to be the state at which the temperature is valid.

Combining Eqs. (1) and (2), the most common form of Mie–Grüneisen equation of states could be obtained [18,19]:

$$p - p_H = \frac{\Gamma}{V}(E_m - E_H) \tag{3}$$

where p_H and E_H are the Hugoniot pressure and specific energy, the Mie–Grüneisen parameter Γ is defined as:

$$\Gamma = \Gamma_0 \frac{\rho_0}{\rho} \tag{4}$$

where Γ_0 is a material constant and ρ_0 is the reference density. The Hugoniot energy, E_H, is related to the Hugoniot pressure by:

$$E_H = \frac{p_H \eta}{2\rho_0} \tag{5}$$

where $\eta = 1 - \rho/\rho_0$ is the nominal volumetric compressive strain. Elimination of Γ and E_H from Eq. (3) yields:

$$p = p_H\left(1 - \frac{\Gamma_0\eta}{2}\right) + \Gamma_0\rho_0 E_m \tag{6}$$

The Mie–Grüneisen equations of state represent coupled equations for pressure and internal energy.

2.1.2. Linear U_s–U_p Hugoniot form

In the absence of pronounced dynamic yielding effects or phase transitions, the hydrostatic pressure is commonly expressed by the Mie–Grüneisen equations of state (Eq. (3)) together with a linear fit assumption for the shock velocity as a function of the particle velocity [20], i.e.:

$$U_s = C_0 + sU_p \tag{7}$$

where U_s represents the shock velocity, C_0 is the zero-pressure isentropic speed of sound, U_p is the velocity of the particle, s is a dimensionless parameter which is related to the pressure derivative of the isentropic bulk modulus. The speed of sound (C_0) of the fluid is inversely proportional to the fluid's compressibility and also to the stable time increment when simulating. With the U_s–U_p equation, the linear U_s–U_p Hugoniot form is then written as:

$$p = \frac{\rho_0 C_0^2 \eta}{(1 - s\eta)^2}\left(1 - \frac{\Gamma_0\eta}{2}\right) + \Gamma_0\rho_0 E_m \tag{8}$$

The limitation of the compression parameters is given by $\eta_{lim} = 1/s$.

In this study, the speed of sound of liquid YSZ was set as 3000 m/s and the dimensionless parameter ***s*** was chosen as 2.39 as illustrated in [21,22].

2.1.3. Temperature dependent viscosity

Due to the low thermal resistance [5] and the large temperature difference between the particle and the substrate, a large temperature gradient develops at the contact interface. As a result, the viscosity in the liquid domain differs considerably affecting the flow and energy dissipation of the liquid. In Vardelle et al. [5] work, an equation to calculate the temperature dependent viscosity of YSZ is provided with further validation by Shinoda et al. [23]:

$$\mu\ (\text{Pa s}) = 0.1e^{\frac{5993}{T}} - 2.95 \tag{9}$$

Table 2. Material properties.

Impinging droplet material	YSZ
Substrate material	Stainless steel (SS)
Substrate initial temperature	423 K
Solidus temperature (YSZ)	2799 K
Liquidus temperature (YSZ)	2801 K
Thermal conductivity (liquid YSZ)	2.00 W/(m K)
Thermal conductivity (solid YSZ)	2.32 W/(m K)
Thermal conductivity (SS)	14.9 W/(m K)
Density (liquid YSZ)	5890 kg/m^2
Density (solid YSZ)	5890 kg/m^2
Density (SS)	7900 kg/m^2
Specific heat capacity (liquid YSZ)	713 J/(kg K)
Specific heat capacity (solid YSZ)	580 J/(kg K)
Specific heat capacity (SS)	477 J/(kg K)
Thermal conductance	5×10^7 W/(m^2 K)
Young's modulus (SS)	200 GPa
Poisson ratio (SS)	0.3
Melting temperature (SS)	1673 K
Room temperature (SS)	293 K
Johnson–Cook fitting parameter A (SS)	310 MPa
Johnson–Cook fitting parameter B (SS)	1000 MPa
Johnson–Cook fitting parameter C (SS)	0.07
Johnson–Cook fitting parameter n (SS)	0.65
Johnson–Cook fitting parameter $\dot{\epsilon}_0$ (SS)	1/s
Johnson–Cook fitting parameter m (SS)	1

Therefore, Eq. (9) was utilized to calculate the viscosity of YSZ at elevated temperatures.

2.1.4. Plastic deformation of solid YSZ

It is known that ceramic materials under normal pressure and temperature behave like brittle material. The material fails as long as the stress reaches the fracture stress right after some elastic deformation. However, Brittle ceramics may become ductile above a specific temperature, which is referred to as brittle-to-ductile transition temperature (BDTT). Below BDTT catastrophic fracture occurs by crack propagation in busting mode whereas above the BDTT, a certain amount of plastic deformation can be obtained prior to the eventual failure. Moreover, some ceramics exhibit superplasticity with an elongation rate exceeding 300%, at temperatures high enough above their BDTTs [24–26]. Therefore, the ceramic core, in the semi-molten simulation, could not be modeled as a pure brittle material since the whole impact process was conducted under relatively high temperature (almost its melting temperature). Thus, certain high-temperature plasticity of YSZ should be defined for the ceramic core. The stress–strain curve from [27] was used to model the plasticity of the YSZ ceramic core for the semi-molten impact case.

2.1.5. Johnson–Cook plasticity model

The elastic response of the material follows a linear elasticity model, which is adequate for most impact cases. The plastic response of stainless steel is assumed to comply with the widely used Johnson–Cook plasticity model [28,29] as follows:

$$\sigma = (A + B\epsilon_p^n)(1 + C\ln\dot{\epsilon}^*)(1 - (T^*)^m) \tag{10}$$

where A, B, n, C and m are material-dependent constants such as static yield strength, strain-hardening exponent, strain-hardening modulus, strain-rate-sensitive coefficient, and thermal-softening exponent. ϵ_p is the effective plastic strain. $\dot{\epsilon}^*$ is the effective plastic strain rate normalized with respect to a reference strain rate $\dot{\epsilon}_p/\dot{\epsilon}_0$. T^* is defined as follows:

$$T^* = \begin{cases} 0 & \text{for} \quad T < T_r \\ \frac{T-T_r}{T_m-T_r} & \text{for} \quad T_r \leqslant T \leqslant T_m \\ 1 & \text{for} \quad T > T_m \end{cases} \tag{11}$$

where T_m is the melting point and T_r is the reference or transition temperature.

Since stainless steel is a widely used metal, the Johnson–cook parameters are easily obtained by experiments and then tested in simulations. The constitutive constants used in this study are provided in Table 2.

3. Results and discussion

3.1. Fully molten droplet impingement

The base line model was applied and validated considering a 30 μm fully molten YSZ droplet impinging onto a stainless steel substrate with an initial velocity of 190 m/s. When a droplet impacts onto a substrate surface, the splat development may follow one of two main processes. The particle may simply impinge, deform intact and then solidify. On the other hand, it may impinge, deform and splash to some degree. This break-up process may be triggered by either low heat transfer to the substrate leading

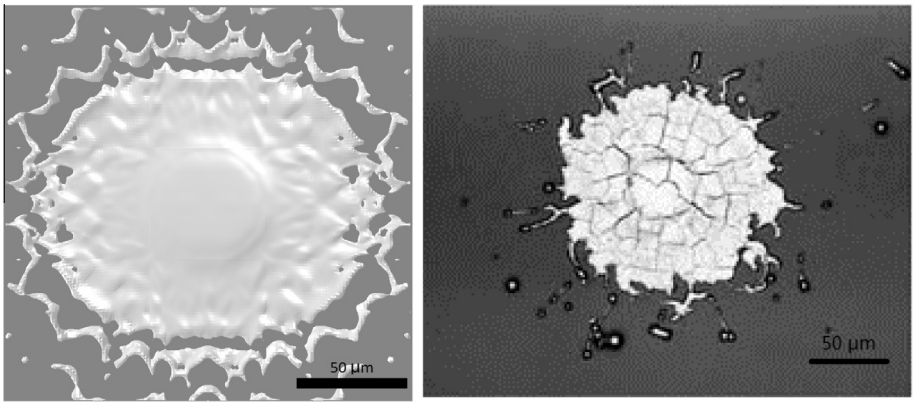

Fig. 3. Comparison between simulated (a) and experimental (b) YSZ droplet impinging onto a SS substrate at temperature of 513 K [3] (top view).

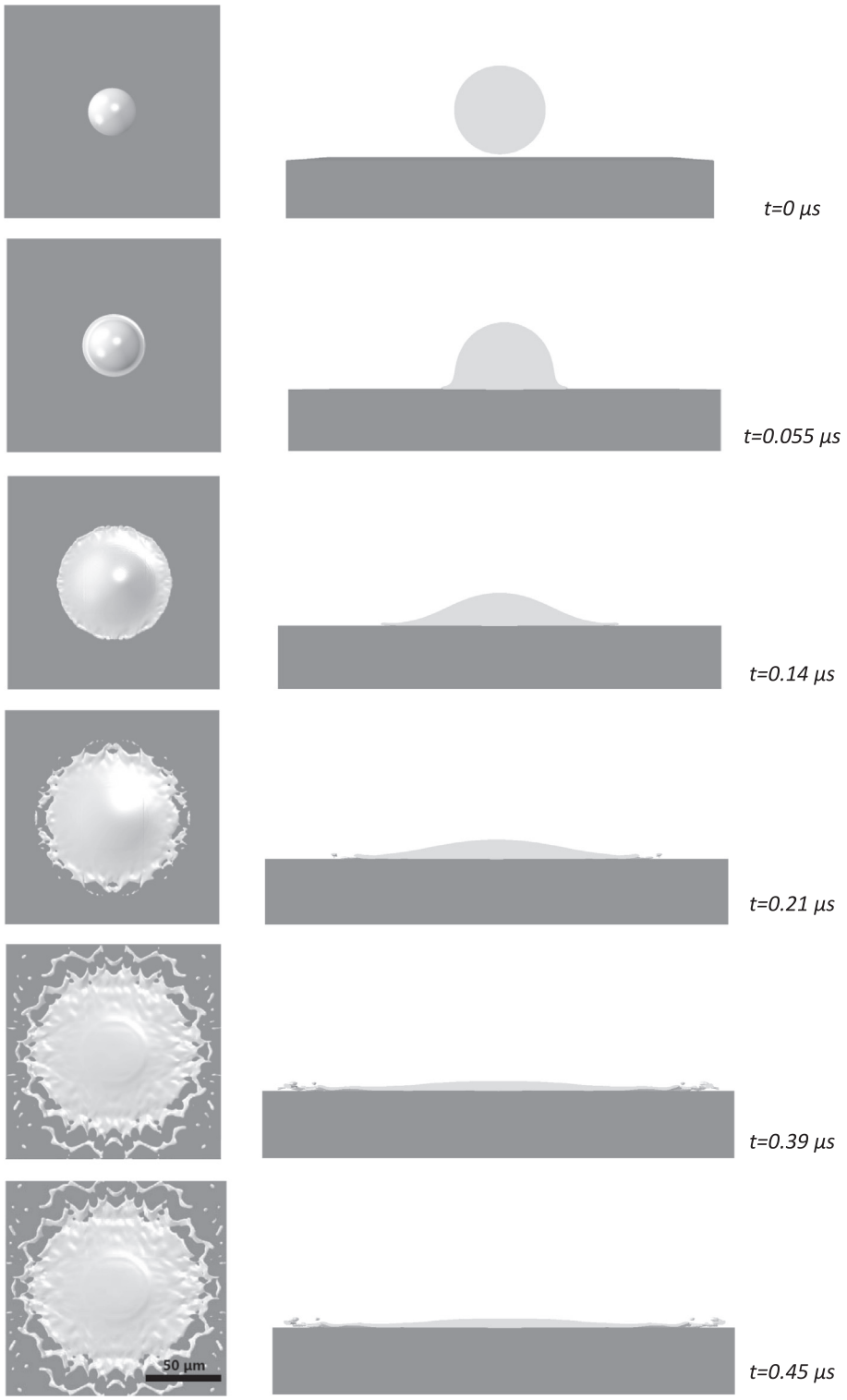

Fig. 4. 30 μm particle impingement process.

to splat fragmentation, or freezing-induced break-up where the heat transfer to the substrate is rapid [30]. The substrate temperature largely determines the splat morphology. A critical temperature termed the transition temperature [31] TT is the temperature below which heat transfer is rapid, leading to freezing-induced break-up. Experimental observations of zirconia droplets impacting onto a quartz glass substrate of temperatures between 300 and 760 K were carried out in [32], leading to a vast difference in final splat morphology patters. For these observations a substrate temperature of 513 K is shown to lie well below the transition temperature, creating a fragmented splat shape due to freezing-induced break-up. In fact, TT is predicted to be $513\ K < TT < 673\ K$. As a result, freezing induced break-up develops during the simulation due to the initial substrate temperature of 513 K, and the final simulated splat

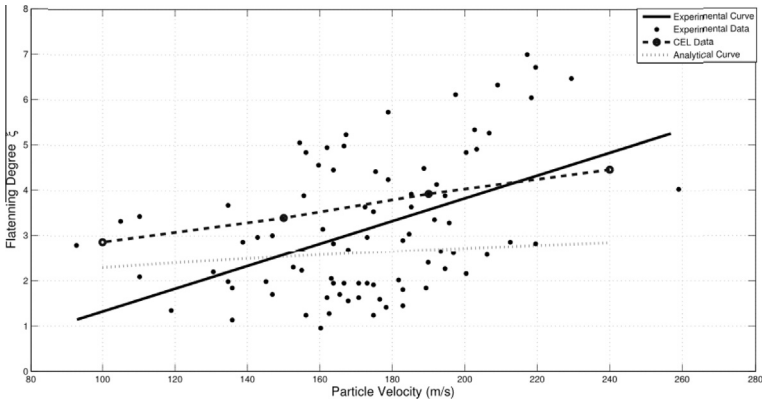

Fig. 5. Comparison among simulated, experimentally measured [5] and analytical calculated [33] flattening degree for the molten YSZ droplet impinging at 190 m/s.

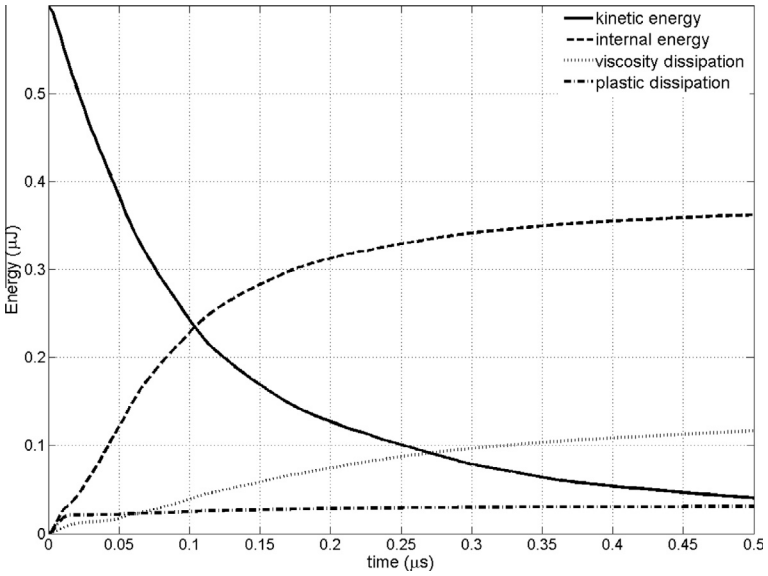

Fig. 6. Energy track for pure liquid droplets with an impact velocity of 240 m/s.

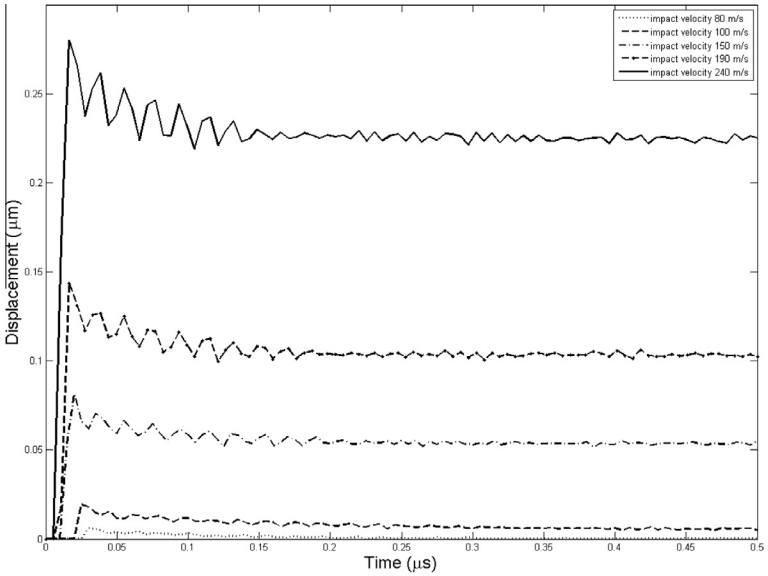

Fig. 7. Displacement of the central node on the contact surface of the substrate at different impact velocities.

morphology is compared alongside the experimental observation in Fig. 3, deposited by hybrid plasma spraying [7]. The two morphologies show a good likeness. An uneven thick central splat remains at the impact site. The splat has an uneven boundary with an undulating circumference consisting of different sized fingers. During the impingement process, the temperature drops dramatically within the contact area resulting in high viscosity levels and rapid solidification of the YSZ. The centrifugal liquid motion is slowed down and eventually a thicker region is developed centrally. The transient motion of the simulated YSZ droplet impacting at 190 m/s is depicted in Fig. 4. The particle impinges onto the surface, where it deforms and begins to spread outward. The molten material then begins to slow and cool due to heat transfer to the substrate. Solidification and retardation at the periphery cause matter to be ejected as Fig. 3 shows. Furthermore, fragmentation is further triggered by the substrate deformation occurring at moderate to high liquid droplet impact velocities. The substrate is slightly deformed, in the form of a smooth shallow crater at the particle–substrate interface, leading to a continually changing direction of the force vector during impact with subsequent impulsive outward liquid ejection followed by fragmentation (Fig. 4).

The quantitative validation of the current model was performed by examining the influence of velocity on the flattening degree. The flattening degree parameter is a normalized number important for the evaluation of the resulting coating quality. The numerical expression of the flattening degree parameter is the diameter of the wetted surface area of the deposition normalized with respect to the initial droplet diameter, see Eq. (12):

$$\xi = \frac{D_{\text{wetted}}}{D_0} \tag{12}$$

A large set of data is collected by varying the impact velocity from 100 to 240 m/s and the flattening degree is calculated based on Eq. (12). The modeling results are compared with experimental data from [5] under identical impact conditions and an empirical formula developed in [33]. By neglecting the contribution of the splat rim on the splat morphology, an empirical formula can be used to describe the particle's flattening degree ξ [33]. ξ is related to the droplet's diameter d, kinematic viscosity υ and the impinging speed V with the following form:

$$\xi = \frac{1}{2}\left(\frac{Vd}{\upsilon}\right)^{\frac{1}{4}} \tag{13}$$

Fig. 5 compares the flattening degree obtained from experiments, the analytical equation and current simulation. Although the experimental splats appear to be randomly impaled, it can be seen that the flattening degree is proportional to the impact velocity as expected. Moreover, Eq. (13) implies that the spread factor ξ is proportional to $V^{1/4}$. The numerical results show a good level of concordance across the specified velocity range.

The energy during the whole impingement was tracked and shown in Fig. 6. Results illustrated that the kinetic energy of the droplet decreased and dissipated in the plastic strain of the substrate as well as the viscosity. Therefore, the deformation of the central node on the contact surface of the substrate was examined and shown in Fig. 7. As can be seen from the displacement–time results, though small, increasing the impact velocity will increase the plastic deformation on the stainless steel on the substrate. Moreover, the influence will become greater at a high initial velocity. Using initial impact velocity of 80 m/s as a datum, the impact velocity was increased by 25%, 88%, 138%, and 300% while the final equivalent plastic strain on the substrate increased by 50%, 210%, 330%, and 680%, respectively. This is based on an elevated initial velocity, more energy was contained in the whole system. Therefore, during the impact process, more energy was transferred and stored by the plastic deformation of the substrate.

3.2. Semi-molten droplet impingement

According to Eq. (13), the degree of flattening ξ increases with particle size increase. However, experiments [7] show that for particles greater than 60 μm, the flattening degree will actually decrease while increasing the particle size (shown in Fig. 8). The thermal gradient within the sphere becomes important for particles larger than 60 μm because the interior resistance to heat flow exceeds that of the plasma gas/powder boundary. In this case, the powder remains in semi-molten form comprising of a liquid shell and a solid core at impact. In this high Biot number case, the CEL computational method was applied by simulating an 80 μm semi-molten YSZ droplet impinging onto a stainless steel substrate with an initial velocity of 190 m/s based on [7].

When the lower part of the liquid shell impacts onto the substrate at $t = 0$, a uniform spread in the radial direction is observed (Fig. 9). The full period of the impact can be divided into two intervals. In the first period, the particle penetrates into the liquid-shell layer adjacent to the sub-

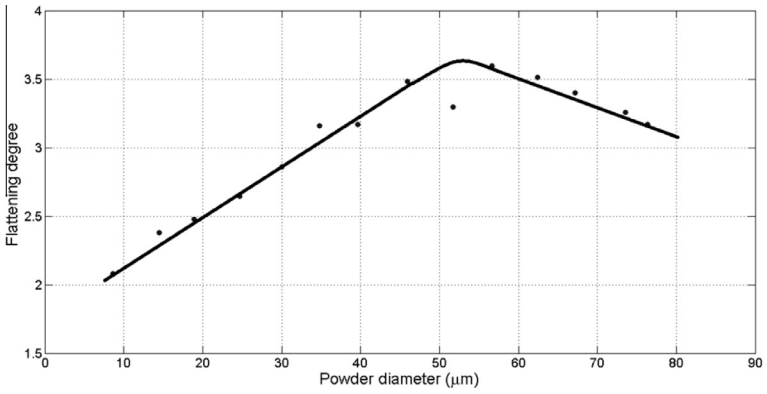

Fig. 8. The dependence of the flattening degree, ξ, on the initial powder diameter d_p [7].

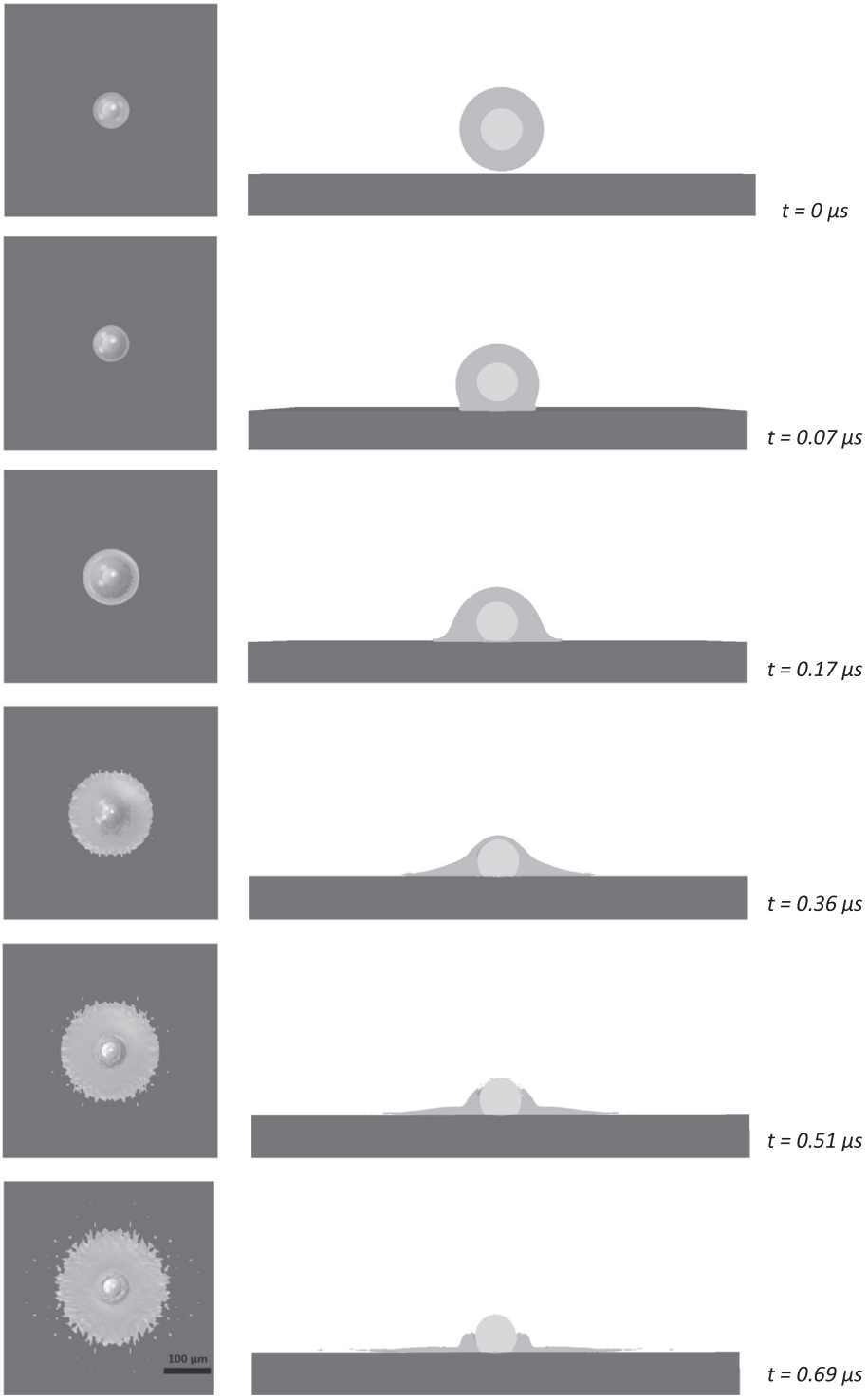

Fig. 9. 80 μm semi-molten YSZ particle with a 40 μm solid core impingement process.

strate and displaces the liquid radially outward. The particle–substrate contact takes place during the second period. At this first stage, the droplets of the liquid shell flows in good contact with the upper hemisphere of the particle upon impact, and separates from the lower hemisphere of the particle when t is approximately 0.17 μs. Beyond this time, break-up of the liquid occurs. At ($0.52\ \mu s < t < 0.69\ \mu s$) the liquid forms two lateral sheet jets, one rushes outward and the other inward toward the symmetry axis. When the inward flowing liquid reaches the particle surface, a part of the liquid volume rebounds upward and breaks up subsequently while the remaining liquid fills in the corner between the particle and the substrate during the spreading. In addition the numerical simulation of the heat transfer and solidification phenomena revealed that solidification of the liquid splat is completed within a time of 0.69 μs and initial impact velocity of 190 m/s. Fig. 9 shows the deformation sequence of an 80 μm droplet with a 40 μm

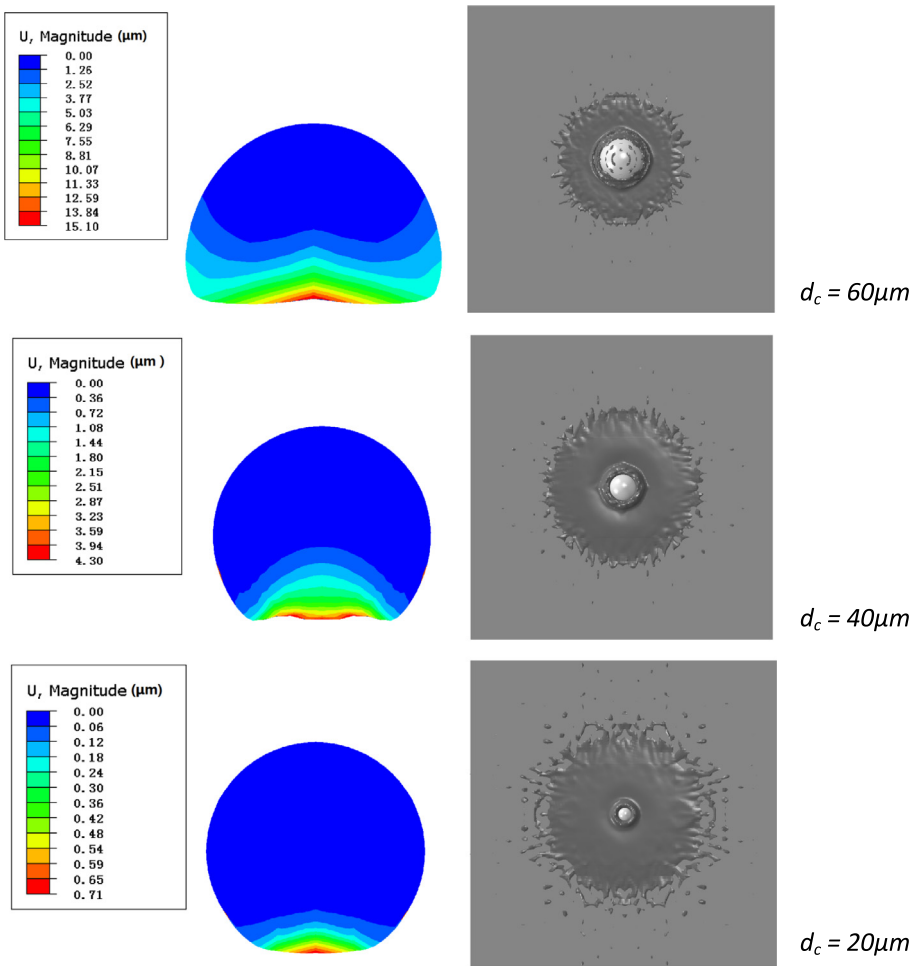

Fig. 10. Deformation of the solid core and top view of splat morphology for semi-molten droplet impact with core sizes of 60, 40, and 20 μm respectively.

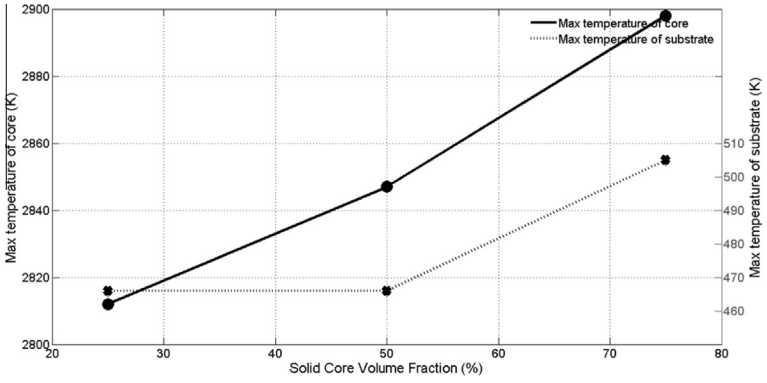

Fig. 11. Maximum temperature during impact on both substrate and solid core.

solid core. In this case no macro-voids will form in the corner between the particle and the substrate.

During the second stage of the process, the solid core comes into contact with the wall. In the early stage of the impingement (0.1 μs), the deformation of the contact surface is evident and the crater size increases in width and height to accommodate the deformed particle. At 0.36 μs, when the solid-core kinetic energy has fallen to zero, the bottom part of the particle is flattened as shown in Fig. 10. The particle experiences a certain deformation with the maximum plastic strain scattering within the contact zone rather than the central point of impact. At the localized solid core-substrate contact interface, temperature increase is observed as a result of the kinetic energy being converted to internal energy and part of it to plastic work (dissipated as heat). The maximum temperature of both

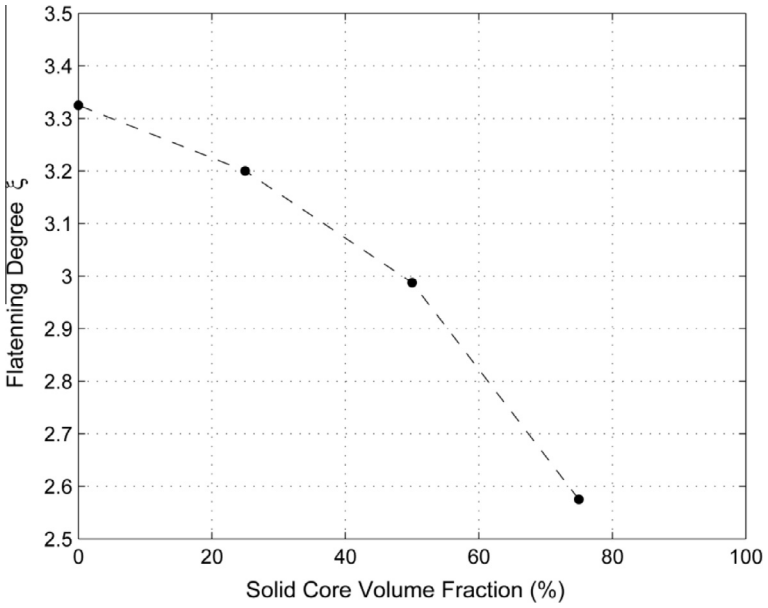

Fig. 12. The effect of core volume fraction on flattening degree, ξ.

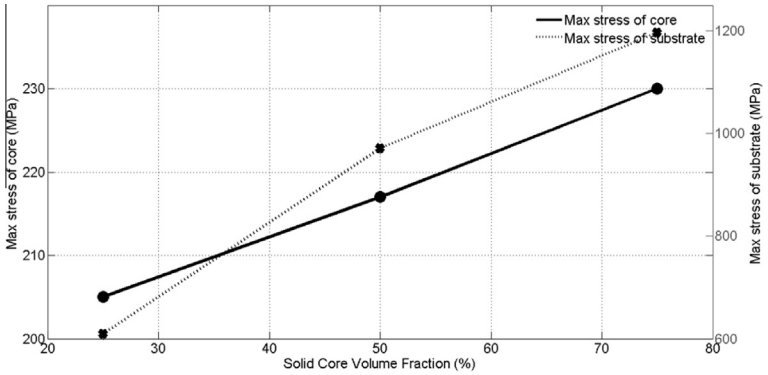

Fig. 13. Maximum stress during impact on both substrate and solid core.

the solid core and the substrate during the adiabatic impact stage could be seen in Fig. 11. The maximum temperature increases along with the increase of the solid volume fraction. The results show that the temperature is not uniformly distributed over the surfaces. A higher temperature is observed along the deformed zones around the edge of the particle than that at the center. The temperature then decreases due to the temperature difference between the solid core and the substrate.

The results show that, in the central part of the contact surface, the liquid shell partially remains at the bottom of the core. Due to the rapid heat exchange between the liquid shell and the substrate, freezing of the central part of the liquid is observed. Thus, the temperature of this domain decreases resulting in solidification and bond of the liquid volume with the substrate. Several other semi-molten droplet impingement cases were performed with the core size ranging from 20 to 60 μm. The final deformation of the solid core and the morphology of the splat can be seen in Fig. 10. The flattening degree is collected and presented in Fig. 12. Comparing the spread factor of the simulation with the experimental results in Fig. 8, the semi-molten flattening degree is approximately 3.1 which can be seen in both experimental [7] and computational results (with 0–25% solid core volume fraction). Furthermore, at higher core volume fraction, the flattening degree decreases dramatically. Also, as shown in Fig. 10, the deformation of the core tends to decrease for smaller core sizes. It can be seen in the same figure that, the larger the core is, the more deformation the core experiences. The top part of the core remains intact while the bottom part starts to deform. Normalizing the maximum deformation on the solid core, U, with the core size, the maximum deformation factor varies from 0.252 to 0.110 and finally to 0.036 with respect to the solid core size of 60 μm, 40 μm and 20 μm. This is a clear indication that the liquid break-up of the shell absorbs the impact energy acting as an opposing damping force. For larger liquid shell thickness, gentler deceleration upon impact is observed attributed to the pressure distribution over a larger area. Overall, it is evident that the thickness of the liquid shell plays an important role on the plastic deformation level of the solid core. Subsequently, the maximum stress on both the substrate and the solid core also varies for different solid volume fractions. As shown in

Fig. 13, a 50% increase in the solid core volume fraction, results in 94% increase of the maximum stress on the substrate and 13% on the particle core.

4. Conclusion

A fully molten and a semi-molten YSZ droplet were simulated to examine the impact onto a solid stainless steel substrate. A 30 μm fully molten ceramic powder with an initial impact velocity of 190 m/s was created as a benchmark. The morphology during the whole process and flattening degree of the deposition were collected. The final splat trend showed good agreements with experimental and analytical results. By increasing the initial impact velocity, the flattening degree increases accordingly as well as plastic deformation on the stainless steel substrate. The higher the velocity is, the larger the plastic strain will be. At the contact interface, the temperature of the liquid decreases, resulting in viscosity increase to stop the flow locally. The solidification completes by forming a thick part in the center of the splat. An 80 μm semi-molten particle with different core size was further simulated. The splat morphology during the whole process was obtained and also the deformation of the solid core was captured. The smaller the solid core is, the larger is the flattening degree found. Also, the normalized deformation factor is proportional to the size of the core.

Acknowledgements

The authors gratefully acknowledge the financial support for this work by the UK Engineering and Physical Sciences Research Council (EPSRC) Project Grants: EP/K027530/1 and FP7 Marie Curie Project Grants: iComFluid 312261 and IPACTS 268696.

References

[1] W.Y. Li, C. Zhang, C.J. Li, H. Liao, J. Therm. Spray Technol. 18 (2009) 92.
[2] W.Y. Li, W. Gao, Appl. Surf. Sci. 255 (2009) 7878.
[3] S. Kamnis, S. Gu, J. Therm. Spray Technol. 19 (2010) 31.
[4] S. Kamnis, S. Gu, T.J. Lu, C. Chen, Comput. Mater. Sci. 46 (2009) 1038.
[5] M. Vardelle, A. Vardelle, A.C. Leger, P. Fauchals, D. Gobin, J. Therm. Spray Technol. 4 (1) (1995) 50.
[6] L. Pwalowski, The Science and Engineering of Thermal Spray Coatings, Wiley, Chichester, 2008.
[7] K. Shinoda, H. Murakami, J. Therm. Spray Technol. 19 (3) (2010) 602.
[8] D. Shi, M. Li, P.D. Christphides, Ind. Eng. Chem. Res. 43 (2004) 3653.
[9] M. Zirari, A. Abdellah El-Hadj, N. Bacha, Appl. Surf. Sci. 256 (2010) 3581.
[10] T.C.M. Wu, M. Bussmann, J. Mostaghimi, J. Therm. Spray Technol. 18 (2009) 957.
[11] H. Tabbara, S. Gu, Appl. Phys. A: Mater. Sci. Process. 104 (2011) 1011.
[12] S. Alavi, M. Passandideh-Fard, J. Mostaghimi, J. Therm. Spray Technol. 21 (6) (2012) 1287.
[13] T. Wu, M. Bussmann, J. Mostaghimi, J. Therm. Spray Technol. 18 (5) (2009) 957.
[14] J. Li, R. Watanabe, Mater. Trans., JIM 40 (1999) 508.
[15] S. Gu, S. Kamnis, Metall. Mater. Trans. A 40 (2009) 2664.
[16] G. Qiu, S. Henke, J. Grabe, SIMULIA Customer Conference, 2009.
[17] K.-M. Shyue, J. Comput. Phys. 171 (2001) 678.
[18] G. Mie, Annalen der Physik. 316.8 (1903), 657.
[19] E. Grüneisen, Annalen der Physik. 344 (12) (1912) 257.
[20] A.L. Ruoff, J. Appl. Phys. 38 (13) (1967) 4976.
[21] T. Mashimo, A. Nakamura, M. Nishida, S. Matsuzaki, K. Kusaba, K. Fukuoka, Y. Syono, J. Appl. Phys. 77 (10) (1995) 5069.
[22] T. Mashimo, A. Nakamura, M. Kodama, K. Kusaba, K. Fukuoka, Y. Syono, J. Appl. Phys. 77 (10) (1995) 5060.
[23] K. Shinoda, Y. Kojima, T. Yoshida, J. Therm. Spray Technol. 14 (4) (2005) 511.
[24] J. Li, R. Watanabe, Mater. Trans., JIM 40 (6) (1999) 508.
[25] F. Wakai, S. Sakaguchi, Y. Matsuno, Adv. Ceram. Mater. 1 (1986) 259.
[26] Y. Maehara, T.G. Langdon, J. Mater. Sci. 25 (1990) 2275.
[27] D. Cheong, J. Lee, Korean J. Mater. Res. 19 (12) (2009) 674.
[28] G.R. Johnson, W.H. Cook, Eng. Fract. Mech. 21 (1985) 31.
[29] G.R. Johnson, W.H. Cook, Proceedings of the 7th International Symposium on Ballistics: (1983) 541–547.
[30] R. Dhiman, A.G. McDonald, S. Chandra, Surf. Coat. Technol. 201 (2007) 7789.
[31] P. Fuchais, M. Fukumoto, A. Vardelle, M. Vardelle, J. Therm. Spray Technol. 13 (2004) 337.
[32] K. Shinoda, H. Murakami, J. Therm. Spray Technol. 19 (2010) 602.
[33] M. Pasandideh-Fard, Y.M. Qiao, S. Chandra, J. Mostaghimi, Phys. Fluids. 8 (1996) 650.